Optimal Operation of a Solar Membrane Distillation Pilot Plant via Nonlinear Model Predictive Control

Juan D. Gil[a], Lidia Roca[b], Alba Ruiz-Aguirre[a], Guillermo Zaragoza[b], Manuel Berenguel[a,*]

[a] *Centro Mixto CIESOL, ceiA3, Universidad de Almería. Ctra. Sacramento s/n, Almería 04120, Spain; {juandiego.gil,ara399,beren}@ual.es*
[b] *CIEMAT-Plataforma Solar de Almería, Ctra. de Senés s/n, Tabernas 04200, Almería, Spain; {lidia.roca,guillermo.zaragoza}@psa.es*

Abstract

Solar Membrane Distillation (SMD) is an under-investigation desalination process suitable for developing self-sufficient small scale applications. The use of solar energy considerably reduces the operating costs, however, its intermittent nature requires a non-stationary optimal operation that can be achieved by means of advanced control strategies. In this paper, a hierarchical control system composed by two layers is used for optimizing the operation of a SMD pilot plant, in terms of thermal efficiency, distillate production and cost savings. The upper layer is formed by a Nonlinear Model Predictive Control (NMPC) scheme, that allows us to obtain the optimal operation by optimizing the solar energy use. The lower layer includes a direct control system, in charge of attaining the variable references provided by the upper layer. Simulation and experimental tests are included and commented in order to demonstrate the benefits of the developed control system.

Keywords: Air-gap membrane distillation, hierarchical control, process control, solar energy, optimization.

1. Introduction

Desalination technologies require intensive generation energy processes for the production of fresh water. For this reason, most of the costs depend directly on the way the energy is obtained and managed. The conventional use of non-renewable energy resources, like fossil fuels, represents a non-sustainable solution from an economic and environmental point of view. Recent research focuses on combining renewable energy sources and desalination processes, as a way of developing efficient and sustainable systems.

*Corresponding author.
Email address: beren@ual.es (Manuel Berenguel)

In this context, Membrane Distillation (MD) is a thermally driven desalination process that can be powered with low grade solar thermal energy (Zaragoza et al., 2014; Cipollina et al., 2012). The main drawback of using solar energy as source is its unpredictable nature, that requires discontinuous operation and the use of specific energy buffering systems. Hence, to develop sustainable SMD commercial systems it is necessary to combine a good technical design and adequate control techniques able to optimize the system operation according to the solar energy behaviour.

There exist numerous examples of the use of offline optimization techniques in the literature aimed at finding optimum operating parameters in terms of thermal efficiency and distillate production. In He et al. (2014), the response surface methodology is used to model an Air Gap Membrane Distillation (AGMD) module. Then, a non-dominated sorting genetic algorithm II was employed to determinate the optimum operating conditions that maximize both distillate production and thermal efficiency. In Khayet & Cojocaru (2012), regression models are proposed to predict the energy module consumption as function of different variables. An optimization problem using Monte-Carlo stochastic methodology was applied in order to maximize the thermal efficiency. However, the optimal operating conditions presented in these works require steady state conditions around the defined points, which are difficult to achieve under real solar-powered operation. As suggested in Gil et al. (2015a,b,c), specific control systems can be used to maintain the main variables of SMD facilities near steady state conditions. From this automatic control point of view, two interesting control approaches are described in Chang et al. (2010, 2012), where a control system formed by conventional Proportional Integral (PI) controllers is employed in order to track optimal operating conditions calculated by means of an offline optimization study focused on maximizing the distillate production. This control system was tested in simulation, obtaining results near the optimum only for clear sky operation. Nevertheless, for coupling desalination processes and solar energy, real time optimization techniques can provide better results in terms of energy efficiency, distillate production and cost savings, since these techniques take into consideration the plant conditions at each sample time. In Karam & Laleg-Kirati (2015) a Newton-based extremum seeking controller is proposed to optimize the permeate flux and the inlet feed according to the variance of the temperature. A dynamic model of the system was used to test the control architecture. The use of a real time optimization system for a real SMD facility has been only addressed by Porrazzo et al. (2013), in which a neural network-based feedforward optimal control system is proposed to maximize the daily production of distillate.

This paper presents a hierarchical control architecture with two layers, focused on optimizing the solar-powered operation of a MD pilot plant. The upper layer includes a Practical Nonlinear Model Predictive Control (PNMPC) strategy (Plucenio et al., 2007) which provides temperature and flow rate setpoints for the heat generation SMD circuit. Besides, a double Exponential Smoothing (DES) technique (NIST, 2006; Pawlowski et al., 2011) combined

with the application of Lagrange interpolation method for signal reconstruction (Pawłowski et al., 2014) has been used to perform irradiance estimation. On the other hand, the lower layer (Gil et al., 2015a,b,c) is formed by PI and feedforward controllers which are in charge of tracking the references calculated by the upper layer. Moreover, two control modes are proposed for the efficient operation of the facility, as well as a start-stop procedure for the solar field and the MD module. In comparison with the work in Porrazzo et al. (2013), the proposed approach has several differences. Whereas in Porrazzo et al. (2013) the feedforward-based controller is used to maximize the distillate production, in the proposed hierarchical control approach different objective functions have been tested (using the same control architecture) allowing to optimize, apart from distillate production, thermal efficiency and cost savings. Additionally, instead of using a complete nonlinear model of the system to determine the optimal operation, the PNMPC strategy calculates an approximated linear model at each sample time. Although this fact can cause a small loss of accuracy, the complexity to solve the optimization problem as well as the computational effort are decreased. The proposed control approach has been tested in the MD-solar pilot plant located at Plataforma Solar de Almería (PSA, www.psa.es), Spain. Simulation and experimental tests are included, showing that the adoption of the proposed control scheme could represent a significant advance towards the development of autonomous commercial SMD systems.

Variable	**Description**	**Units**
DT1	Distillate production	L/min
FT1	Solar field water flow rate	L/min
FT2	Water flow rate between the tank and the distribution system	L/min
FT3	Heat exchanger water flow rate	L/min
FT4	Feed water flow rate	L/min
I	Global irradiance measured at 36^o tilted	W/m^2
T_a	Ambient temperature	^{o}C
TT1	Solar field inlet temperature	^{o}C
TT2	Solar field outlet temperature	^{o}C
TT3	Temperature at the top of the tank	^{o}C
TT4	Distribution system inlet temperature	^{o}C
TT5	Heat exchanger inlet temperature, hot side	^{o}C
TT6	Heat exchanger outlet temperature, hot side	^{o}C
TT7	Distribution system outlet temperature	^{o}C
TT8	Temperature at the bottom of the tank	^{o}C
TT9	Heat exchanger inlet temperature, cold side	^{o}C
TT10	Heat exchanger outlet temperature, cold side	^{o}C
TT11	Feed water temperature	^{o}C

Table 1: Variables monitored in the SMD facility.

2. MD-solar pilot plant

2.1. The MD technology

MD consists on a thermally-driven desalination process that uses a hydrophobic micro-porous membrane to separate the water vapour from sea or brackish water. The driving force of the process is the pressure gradient originated at both membrane sides, which is achieved by a temperature difference. In consequence, volatile molecules are evaporated and transported through the porous membrane whereas non-volatile compounds are rejected. The vapour can then be condensed inside the module or outside in an external condenser, depending of the MD configuration employed (Alkhudhiri et al., 2012). The most adopted configurations are Direct Contact Membrane Distillation (DCMD), Permeate Gap Membrane Distillation (PGMD) and AGMD, in which condensation takes place inside the module, and Sweeping Gas Membrane Distillation (SGMD) and Vacuum Membrane Distillation (VMD), where condensation occurs outside the module in an external device.

MD systems have several advantages that make this technology specially suitable for developing self-sufficient small scale desalination applications. Among the several advantages, the main ones are: (1) an intensive pre-treatment of the feed water is not required, just a simple filtration process; (2) the simplicity of the process reduces the maintenance requirements and enables easy automation; (3) it can be operated under intermittent conditions without damaging the membrane; (4) the operating temperature is low, between 60-85 ^{o}C. Particularly, the last two make possible the use of solar energy as source, thus enabling the development of efficient autonomous systems (Zaragoza et al., 2014; Cipollina et al., 2012).

2.2. The SMD pilot plant

The SMD pilot plant at PSA (Zaragoza et al., 2014; Ruiz-Aguirre et al., 2017b) is formed by an AGMD module and a heat generation circuit which comprises a solar thermal field, a storage tank and a distribution system (see Fig. 1).

The MD commercial unit (built by Aquastill) consists on a spiral wound module based on the AGMD technology (Alkhudhiri et al., 2012). The effective surface area is 24 m^2 with a length of 5 m. Productivity tests and a full characterization of the AGMD module were presented in (Ruiz-Aguirre et al., 2015). The unit has its own heat exchanger, which is used to warm up the feed water, which is preheated after acting as a coolant in the condenser channel of the module, with the fluid coming from the heat generation circuit.

The required thermal energy is provided by a solar field formed by stationary flat-plate collectors Solaris CP1 Nova purchased from Solaris (Spain), which are set in two rows of five collector each one. A complete description of the solar field was presented in (Zaragoza et al., 2014). The facility is also equipped with a thermal storage tank (1500 L) that is used as energy buffer device to store and manage the thermal energy coming from the solar field. The storage tank permits the operation of the plant in several modes, as it was described

in Gil et al. (2015a). In this paper the MD module is fed by the storage tank, which is heated by recirculating the fluid through the solar field (see Section 2.3). Finally, a distribution system is available to connect the heat generation circuit and the MD module. Notice that the distribution system enables the simultaneous connection of several MD units.

The plant is completely monitored and controlled trough a Programmable Logic Controller (PLC) and a Supervisory Control And Data Acquisition (SCADA) system with a sample time of 1 s. All the monitored variables are presented in Tab. 1. Details about instrumentation can be found in Zaragoza et al. (2014); Gil et al. (2015a).

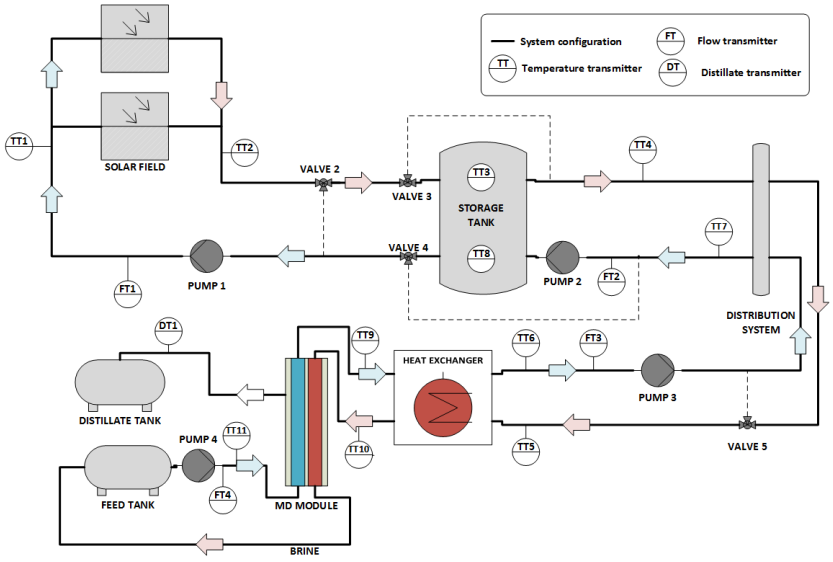

Figure 1: Schematic diagram of the plant.

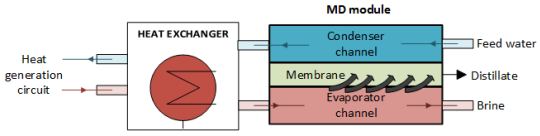

Figure 2: Schematic diagram of the MD module.

2.3. System configuration and nominal operating ranges

As it has been highlighted before, the SMD plant can be operated in different modes (Gil et al., 2015a). In this case, the fluid coming from the solar field flows directly to the tank, which is used to feed the module. By using this operating mode, the continuity of the operation is improved, since most of the transients

caused by irradiance disturbances are attenuated by the buffer system. In addition, in this paper, only the solar-powered operation is investigated, assuming that there are not other thermal sources.

On the other hand, pump 4 (see Fig. 1) drives feed water into the condenser channel of the module (see Fig. 2). This feed flow rate varies between 400 and 600 L/h, that is the maximum allowed by the module. Moreover, the feed tank temperature is kept at 20 ^{o}C and the salinity is 35 g/L, representing mean values of the seawater conditions adopted in this work. Once the feed water reaches the heat exchanger, it is heated with the recirculating fluid coming from the heat generation circuit. Then, the hot feed water flows into the evaporator channel of the module. The inlet evaporator temperature varies from 60 to 84 ^{o}C, since temperatures lower than 60 ^{o}C produce very low distillate flow, and 84 ^{o}C is the maximum allowed by membrane materials. The volatile molecules of the hot feed water are evaporated in the evaporator channel and pass trough the membrane, whereas the non-volatile components exit from the evaporator channel as brine. The volatile molecules are then condensed in contact with the condensation foil of the membrane, thus transferring some of the heat to the feed water that circulates in the condensation channel, which is pre-heated before reaching the heat exchanger. It should be noted that both the brine and the distillate are returned to the feed tank, which causes an increase of the temperature during the operation. Thus, an auxiliary tank equipped with a chiller is used to keep the desired feed tank conditions.

3. System modeling

In order to achieve a successful implementation of the PNMPC control system, it is necessary to develop a model which accurately represents the behaviour of the facility. According to the SMD plant configuration, the model has to include the solar field, thermal storage tank, distribution system, heat exchanger, pump 1, pump 2, pump 3 and MD module. It should be taken into account that the model of the heat generation circuit has been already presented and validated in (Gil et al., 2015a,b,c). The definition of all the parameters used in equations (1)-(13) is presented in Tab. 2 (those not included in Tab. 1).

Thus, the solar field was modeled using the lumped-parameters model included in Roca et al. (2009), that is given by:

$$A_{sf}\cdot\rho\cdot c_p\cdot\frac{\partial \mathrm{TT2}(t)}{\partial t} = \beta\cdot \mathrm{I}(t) - \frac{H}{L_{eq}}\cdot(\bar{T}(t) - \mathrm{T}_a(t)) - c_p\cdot\dot{m}_{eq}\cdot\frac{\mathrm{TT2}(t) - \mathrm{TT1}(t)}{L_{eq}}, \quad (1)$$

where:

$$L_{eq} = L_a \cdot n_{cs}, \quad (2)$$

$$\dot{m}_{eq} = \frac{\mathrm{FT1}\cdot\rho}{c_1}, \quad (3)$$

$$\bar{T}(t) = \frac{\mathrm{TT1}(t) + \mathrm{TT2}(t)}{2}. \quad (4)$$

Variable	Description	Units
A_{he}	Heat exchanger area	1.65 m^2
A_{sf}	Collector absorber cross-section area	0.007 m^2
c_1	Conversion factor to account for connections, number of modules and L/min conversion	$9 \cdot 2 \cdot 6 \cdot 10^4$ $(s \cdot L)/(min \cdot m^3)$
c_2	Conversion factor to kWh	$3.6{\cdot}10^6$ J/kWh
c_p	Specific heat capacity of demineralized water	J/(kg·^{o}C)
$c_{p,sw}$	Specific sea water heat capacity	J/(kg·^{o}C)
F	Input frequency	%
H	Solar field global thermal losses coefficient	5.88 J/(s·K)
k	Static gain of FOPDT transfer functions	
L_a	Collector absorber tube length	1.95 m
L_{eq}	Equivalent absorber tube length	9.75 m
$\dot{m}_{ds}$	Water mass flow rate between the tank and the distribution system	kg/s
$\dot{m}_{eq}$	Equivalent solar-field mass flow rate	kg/s
$\dot{m}_{sf}$	Water mass flow rate between the tank and the solar field	kg/s
$\dot{m}_1$	Heat generation circuit mass flow rate	kg/s
$\dot{m}_2$	MD module circuit mass flow rate	kg/s
n_{cs}	Number of series-connections in a collectors group	5
$\bar{T}$	Equivalent absorber tube mean temperature	^{o}C
$TT6_m$	TT6 estimated by the model	^{o}C
$TT10_m$	TT10 estimated by the model	^{o}C
t_d	Representative time delay of FOPDT transfer functions	s
UA_1	Tank thermal losses coefficient, lower part	3.6 J/(s·K)
UA_2	Tank thermal losses coefficient, upper part	3.8 J/(s·K)
V	Tank volume	1.5 m^3
α_{he}	Heat exchanger heat transfer coefficient	670.80 W/(m^2·K)
β	Irradiance model parameter	0.11 m
ΔT	Temperature difference between TT10 and TT9	^{o}C
η_{he}	Heat exchanger auxiliary factor	–
τ	Representative time constant of FOPDT transfer functions	s
θ_{he}	Heat exchanger auxiliary factor	–
ρ	Demineralized water density	kg/m^3
ρ_{feed}	Feed water density	kg/m^3

Table 2: Model parameters.

A two-nodes stratified dynamic model was employed for the storage tank, as suggested in Duffie & Beckman (1980):

$$\begin{aligned}\frac{\partial \mathrm{TT3}(t)}{\partial t} = \frac{1}{\rho \cdot V} \cdot \big(&\dot{m}_{sf} \cdot \mathrm{TT2}(t) + \dot{m}_{ds} \cdot \mathrm{TT8}(t) - \dot{m}_{sf} \cdot \mathrm{TT3}(t) \\ &- \dot{m}_{ds} \cdot \mathrm{TT3}(t) - \frac{\mathrm{UA}_1 \cdot (\mathrm{TT3}(t) - \mathrm{T}_a(t))}{c_p}\big),\end{aligned} \tag{5}$$

$$\begin{aligned}\frac{\partial \mathrm{TT8}(t)}{\partial t} = \frac{1}{\rho \cdot V} \cdot \big(&\dot{m}_{sf} \cdot \mathrm{TT3}(t) + \dot{m}_{ds} \cdot \mathrm{TT7}(t) - \dot{m}_{sf} \cdot \mathrm{TT8}(t) \\ &- \dot{m}_{ds} \cdot \mathrm{TT8}(t) - \frac{\mathrm{UA}_2 \cdot (\mathrm{TT8}(t) - \mathrm{T}_a(t))}{c_p}\big).\end{aligned} \tag{6}$$

A first principles-based static model was used to characterize the heat exchanger, according to the ideas presented in de la Calle et al. (2016):

$$\mathrm{TT6}_m = \mathrm{TT5} - \eta_{he,1} \cdot (\mathrm{TT5} - \mathrm{TT9}), \tag{7}$$

$$\mathrm{TT10}_m = \mathrm{TT9} + \eta_{he,2} \cdot (\mathrm{TT5} - \mathrm{TT6}_m), \tag{8}$$

where:

$$\eta_{he,1} = \frac{1 - e^{\theta_{he}}}{1 - \frac{\dot{m}_1 \cdot c_p}{\dot{m}_2 \cdot c_{p,sw}} e^{\theta_{he}}}, \tag{9}$$

$$\eta_{he,2} = \frac{\dot{m}_1 \cdot c_p}{\dot{m}_2 \cdot c_{p,sw}}, \tag{10}$$

$$\theta_{he} = \alpha_{he} \cdot A_{he} \cdot \left(\frac{1}{\dot{m}_1 \cdot c_p} - \frac{1}{\dot{m}_2 \cdot c_{p,sw}}\right). \tag{11}$$

Moreover, a first order filter and a time delay have been added to this static model to fit real response data. The representative time constant is 40 s and the time delay is 23 s for $\mathrm{TT6}_m$, whereas the time constant is 20 s and the time delay is 15 s for $\mathrm{TT10}_m$.

The distribution system was modeled by means of a static energy balance, taking into account that in a normal operation, with FT2 higher than FT3, a mixture is produced between the fluid coming from the tank and the cold fluid coming from the heat exchanger:

$$\mathrm{TT7} = \frac{\mathrm{TT4} \cdot (\mathrm{FT2} - \mathrm{FT3}) + \mathrm{TT6} \cdot \mathrm{FT3}}{\mathrm{FT2}}. \tag{12}$$

Besides, as in the previous case, a low pass filter has been added to the output of Eq. 12 with a representative time constant of 7 s based on experimental results.

Pumps were modeled trough First Order Plus Dead Time (FOPDT) transfer functions obtained from experimental data, see Tab. 3.

$G(s)$	$Y(s)$	$U(s)$	k	τ [s]	t_d [s]
$G_1(s)$	FT1(s)	$\mathrm{F_{P1}}(s)$	0.2344	5	1
$G_2(s)$	FT2(s)	$\mathrm{F_{P2}}(s)$	0.1674	7.65	3.01
$G_3(s)$	FT3(s)	$\mathrm{F_{P3}}(s)$	0.1345	8.03	3

Table 3: Transfer functions obtained from experimental data.

Finally, an experimental campaign was carried out to obtain a static model of the AGMD module distillate production (DT1) and ΔT, that is the difference between the inlet evaporator channel temperature (TT10) and the outlet condensation channel temperature (TT9). More details about the experimental procedure were shown in (Ruiz-Aguirre et al., 2015).

$$\begin{aligned}\mathrm{DT1} = 24 \cdot (0.135 + 0.003 \cdot \mathrm{TT10} - 0.0204 \cdot \mathrm{TT11} - 0.001 \cdot \mathrm{FT4} \\ + 0.00004 \cdot \mathrm{TT10} \cdot \mathrm{FT4}),\end{aligned} \tag{13}$$

$$\triangle \mathrm{T} = -0.739 + 0.078 \cdot \mathrm{TT10} - 0.067 \cdot \mathrm{TT11} + 0.0019 \cdot \mathrm{FT4}. \tag{14}$$

4. Optimal operation of the MD module

When coupling a thermal desalination process with solar energy, the plant thermal efficiency is an essential factor. It should be noted that the thermal efficiency varies according to the MD configuration and module design. Thus, the optimal operation strategy in terms of energy efficiency as well as distillate production should be characterized for each MD module. Several performance indices can be adopted to evaluate thermal efficiency, being the Specific Thermal Energy Consumption (STEC), which is widely employed in the literature to evaluate the energy consumption of MD systems (Duong et al., 2016; Guillén-Burrieza et al., 2012; Zaragoza et al., 2014; Ruiz-Aguirre et al., 2017a,b), the one used in this work:

$$\mathrm{STEC}\ [\mathrm{kWh/m^3}] = \frac{\mathrm{FT4} \cdot \rho_{feed} \cdot c_{p,sw} \cdot \Delta \mathrm{T}}{c_2 \cdot \mathrm{DT1}}, \tag{15}$$

this index provides the thermal energy required per volume of distillate produced.

In order to observe the influence of each variable in the STEC value and to assess the optimal operation of the AGMD module employed in this work, 3D response surface plots have been displayed. The performance of STEC, ΔT and DT1 have been evaluated with respect to the inlet evaporation channel temperature (TT10) and the feed water flow rate (FT4), maintaining TT11 fixed at 20 ^{o}C (mean seawater temperature considered in this work).

Fig. 3 shows the 3D distillate flow rate response surface plot. It can be seen that the distillate production flow rate augments when FT4 and TT10 increase. Nevertheless, TT10 affects more significantly than FT4. Moreover, in

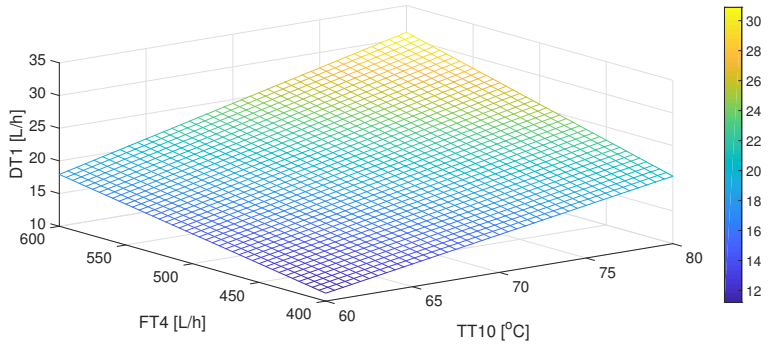

Figure 3: 3D response surface plot of distillate flow rate.

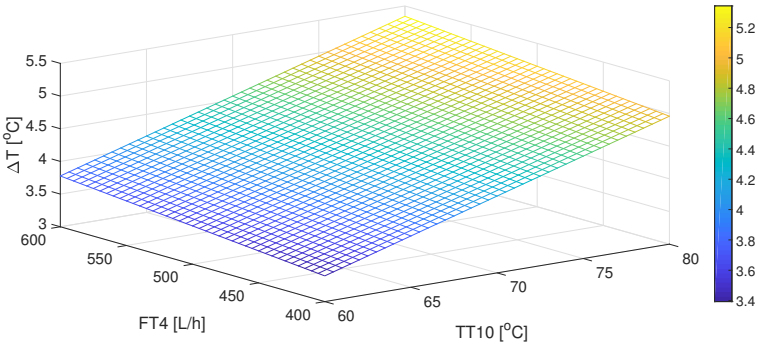

Figure 4: 3D response surface plot of ΔT.

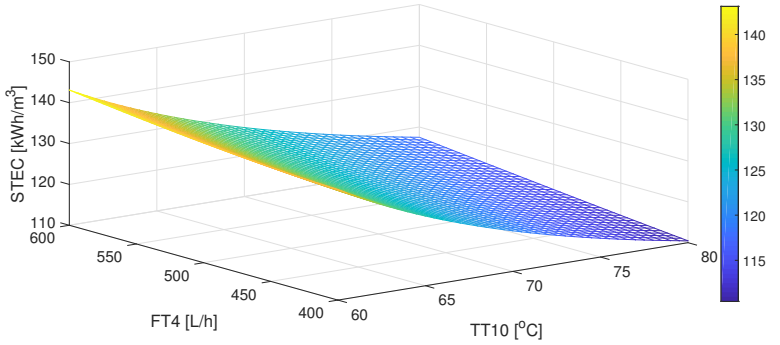

Figure 5: 3D response surface plot of STEC.

accordance with Eq. 15, STEC is a function of FT4, DT1 and ΔT. Fig. 4 and 5 show the effects of TT10 and FT4 in ΔT and STEC. It should be taken into account that TT10 has more influence than FT4 in both parameters. Besides, although ΔT increases when high TT10 is applied (see Fig. 4), DT1 increases more significantly (see Fig. 3). This fact reduces STEC, which implies a greater thermal efficiency in the operation.

Hence, to obtain an optimal operation in terms of thermal efficiency and distillate production, the temperature should be the highest reachable one by the heat generation circuit at each instant, taking into account that this temperature varies in accordance with the operating conditions. On the other hand, the minimum STEC and the maximum distillate production is achieved with low and high FT4, respectively. Nevertheless, the distillate flow rate production difference achieved when the maximun and minimum FT4 is applied, is much greater than the STEC one, from 17.8 to 28.44 L/h for the distillate flow rate and from 117.2 to 119.6 kWh/m^3 for the STEC. Therefore, FT4 will be operated at 600 L/h in order to achieve the maximum flow rate of distillate.

5. Control system architecture

After the previous analysis, it has been concluded that the key for the optimal operation of the SMD facility is the proper management of temperature TT10, by means of the heat generation circuit. For this purpose, the two chosen controlled variables are TT2 and FT2, which enable to control the thermal power to load and unload the tank. It should be considered that FT2 has a significant influence in the inlet solar field temperature as well as in the outlet distribution system temperature, due to the mix produced in the distribution system and in the lower part of the tank. This fact produces that its operation is not trivial, thus justifying its inclusion in the control system.

On the other hand, to obtain a profitable economic balance of the plant, pump 2, 3 and 4 should not be operated when TT10 is lower than 60 ^{o}C, since the MD module produces very low distillate flux in comparison with the electric consumption of pumps. In this way, two different control modes are proposed. The first one consists on a tank fast heating mode, in which the PNMPC strategy optimizes the solar field outlet temperature (TT2) in order to warm up the tank quickly, until reaching a temperature that allows us to operate the MD module with 60 ^{o}C. The second one is the normal operating mode, which is used as long as the MD module is operated. When this mode is selected, the control system acts on TT2 and FT2 setpoints ($TT2_{SP}$ and $FT2_{SP}$) according to the two different objective functions proposed for this mode. The switching mechanism (decision maker in Fig. 6) between both modes is based on the start-stop procedure explained in Section 5.4 and 5.5.

Therefore, the proposed control architecture (see Fig. 6) consists on a classical hierarchical control system, in which the optimization layer, the top one, acts as reference governor, by using a PNMPC strategy (Plucenio et al., 2007) providing temperature and flow rate references. Besides, a DES technique (Pawlowski

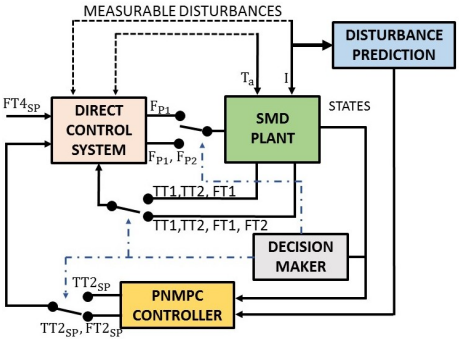

Figure 6: Hierarchical control strategy scheme.

et al., 2011) is used to predict the irradiance and to improve the system behaviour estimation. The inner layer, which is composed by a direct control system, manipulates the input frequency of pump 1 and 2 (F_{P1} and F_{P2}) to maintain the setpoints calculated by the upper layer in spite of irradiance disturbances.

5.1. Lower layer: Direct control system

The direct control layer includes two loops, and all the details about its configuration were presented in Gil et al. (2015a,b,c). The aim of this control layer is to maintain the two controlled variables, TT2 and FT2, near steady state conditions despite disturbances, which mainly are ambient temperature (T_a), inlet solar fiel temperature (TT1) and global irradiance (I). Firstly, TT2 is controlled using a cascade control loop (see Fig. 7), acting in the input frequency of pump 1 (F_{P1}). Besides, a feedforward (FF) that uses a static version of the solar field model (see Section 3), provides the nominal flow rate FT1 in accordance with irradiance disturbances and operating conditions. A Low Pass Filter (LPF) has been added to this static FF to achieve a better dynamical behaviour and a smooth response. In the same way, a LPF has been also included in the reference signal to find a good tradeoff between reference tracking and disturbances rejection and to reduce overshoots against setpoint step changes. The representative closed-loop time constant of this controller is 72 s.

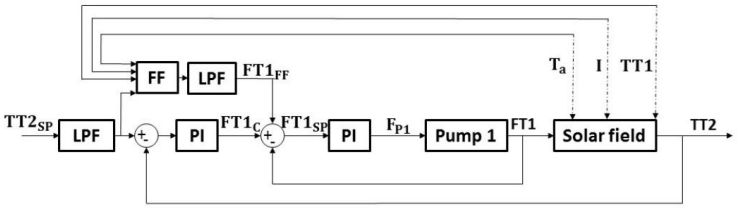

Figure 7: Solar field control scheme. $FT1_{FF}$ is the FF control signal and $FT1_c$ is the feedback control signal.

Secondly, a classical feedback loop with a PI controller (see Fig. 8) is employed to control the feed flow rate FT2 by means of the input frequency of pump 2 (F_{P2}). In this occasion, the representative closed-loop time constant is 6.5 s.

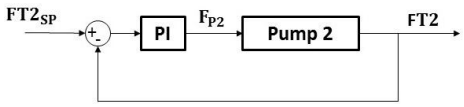

Figure 8: FT2 control scheme.

Notice that an antiwindup scheme was added to each control loop. Pump 1 values range from 7.5 to 16 L/min and the pump 2 one from 15 to 25 L/min. This direct control layer has been implemented with a sample time of 5 s, allowing the solar field control loop detecting irradiance changes quickly. It should be mentioned that the original control architecture presented in Gil et al. (2015a,b,c) also includes a temperature control loop aiming at controlling the temperature at the inlet of the heat exchanger, by acting on valve 5. However, in this work, instead of using this control loop, valve 5 is kept fully open and it acts only commanded by means of a security mechanism that closes the valve when the temperature coming from the distribution system is higher than 95 ^{o}C, avoiding damages in the membrane.

5.2. Upper layer: PNMPC strategy

As it has been pointed out before, the optimization layer manages the thermal energy storage in the tank by generating appropriate setpoints to the outlet solar field temperature ($TT2_{SP}$) and to the feed flow rate FT2 ($FT2_{SP}$), according to the selected control mode and the objective function employed in the normal operating mode. For this purpose, a PNMPC strategy has been adopted (Plucenio et al., 2007), which has already been successfully tested in other nonlinear systems (Castilla et al., 2014; Álvarez et al., 2013), being also possible to increase robustness of the approach by filters shown in Andrade et al. (2013).

PNMPC algorithms are identified by the use of a vector $\hat{\mathbf{Y}}$ that includes predictions of the future system outputs in a determined prediction horizon N, as a function of the future movements of the control signal $\mathbf{\Delta U}$:

$$\hat{\mathbf{Y}} = \mathbf{F} + \mathbf{G} \cdot \mathbf{\Delta U}, \tag{16}$$

where $\mathbf{F}$ is the free response and $\mathbf{G}\cdot\mathbf{\Delta U}$ is the forced response. In linear MPC algorithms, $\hat{\mathbf{Y}}$ is estimated using a linear model of the system at hand. However, in the PNMPC control approach, $\hat{\mathbf{Y}}$ is calculated using the nonlinear SMD plant model presented in Section 3. It should be mentioned that, in order to save computational time, difference equations have been employed for the solar field and tank models instead of the differential ones.

Firstly, in the tank fast heating mode (related with J1, see Section 5.2.1), the input used for the PNMPC technique ($\mathbf{U}_{J1}$) are the actual and future values of

$TT2_{SP}$, whereas the output ($\hat{\mathbf{Y}}_{J1}$) includes the future predicted values of TT3. Thus, the PNMPC formulation for the first control mode is given by:

$$\hat{\mathbf{Y}}_{J1} = \mathbf{F} + \mathbf{G}_{PNMPC} \cdot \boldsymbol{\Delta}\mathbf{U}, \tag{17}$$

where

$$\boldsymbol{\Delta}\mathbf{U} = \boldsymbol{\Delta}\mathbf{U}_{J1}, \tag{18}$$

$$\mathbf{F} = f(\mathbf{y_{J1,p}}, \boldsymbol{\Delta}\mathbf{u_{J1,p}}, \boldsymbol{\Delta}\mathbf{v_p}), \tag{19}$$

$$\mathbf{G}_{PNMPC} = \left[\begin{array}{c} \frac{\partial \hat{\mathbf{Y}}_{J1}}{\partial \mathbf{U}_{J1}} \end{array} \right], \tag{20}$$

$\mathbf{y_{J1,p}}$, $\boldsymbol{\Delta}\mathbf{u_{J1,p}}$ and $\boldsymbol{\Delta}\mathbf{v_p}$ are sets of past values of outputs, inputs and disturbances respectively.

Secondly, the two chosen input vectors of actual and future control actions, $\mathbf{U_1}$ and $\mathbf{U_2}$, for the normal operating mode (related with J2 and J3, see Section 5.2.1) are $\mathbf{TT2}_{SP}$ and $\mathbf{FT2}_{SP}$ respectively, whereas the predicted output vector, $\hat{\mathbf{Y}}$, is $\mathbf{TT10}$. Thus, the PNMPC formulation is:

$$\hat{\mathbf{Y}} = \mathbf{F} + \mathbf{G}_{PNMPC} \cdot \boldsymbol{\Delta}\mathbf{U}, \tag{21}$$

$$\mathbf{F} = f(\mathbf{y_p}, \boldsymbol{\Delta}\mathbf{u_p}, \boldsymbol{\Delta}\mathbf{v_p}), \tag{22}$$

$$\boldsymbol{\Delta}\mathbf{U} = [\boldsymbol{\Delta}\mathbf{U}_1;\ \boldsymbol{\Delta}\mathbf{U}_2], \tag{23}$$

$$\mathbf{G}_{PNMPC} = \left[\begin{array}{cc} \frac{\partial \hat{\mathbf{Y}}}{\partial \mathbf{U_1}} & \frac{\partial \hat{\mathbf{Y}}}{\partial \mathbf{U_2}} \end{array} \right], \tag{24}$$

$\mathbf{y_p}$, $\boldsymbol{\Delta}\mathbf{u_p}$ and $\boldsymbol{\Delta}\mathbf{v_p}$ are sets of past values of outputs, inputs and disturbances respectively.

It should be taken into account that this technique provides only an approximation of the predictions, nevertheless it reproduces better the system performance than a linear model, due to $\mathbf{G}_{PNMPC}$ being computed using linearized models at each instant, while $\mathbf{F}$ is estimated with the nonlinear model, maintaining the future control movements constants and using the prediction of the measurables disturbances (see Section 5.3). Thus, to calculate $\mathbf{F}$ and $\mathbf{G}_{PNMPC}$ for each control mode at each sample time, the algorithm presented in Algorithm 1 and described in Plucenio et al. (2007) should be used. Additionally, as pointed out in Plucenio et al. (2007); Andrade et al. (2013), for the treatment of disturbances, prediction errors and noises, the implementation of the PNMPC algorithm in this work uses an explicit form of generalized predictive control where the integral of the filtered prediction error is added to the predicted system output to correct open loop predictions (not explicitly included in Algorithm 1 for the sake of simplicity).

Algorithm 1 Procedure to estimate $\mathbf{F}$ and $\mathbf{G}_{\mathrm{PNMPC}}$

1. To obtain $\hat{\mathbf{Y}}^0$, which is a vector of N elements, where N is the prediction horizon, the model should be executed using past inputs, outputs and the prediction of the measurable disturbances (see Section 5.3), with $\mathbf{\Delta U}^a$=[0 0...0]^t. So that, $\mathbf{F} = \hat{\mathbf{Y}}^0$.
2. To calculate the first column of $\mathbf{G}_{\mathrm{PNMPC}}$. $\hat{\mathbf{Y}}^1$ is obtained as it has been detailed in the previous step, but in this case $\mathbf{\Delta U}$=[ϵ 0...0]^t, where $\Delta\mathbf{u^i}$ is a small increment in the control signal, e.g. $\frac{u(k-1)}{1000}$. $\mathbf{G}_{\mathrm{PNMPC}}(:,1)=\frac{\hat{\mathbf{Y}}^1-\hat{\mathbf{Y}}^0}{\epsilon}$.
3. The second column of the $\mathbf{G}_{\mathrm{PNMPC}}$, is estimated by calculating $\hat{\mathbf{Y}}^2$ with $\mathbf{\Delta U}$=[0 ϵ...0]^t. $\mathbf{G}_{\mathrm{PNMPC}}(:,2)=\frac{\hat{\mathbf{Y}}^2-\hat{\mathbf{Y}}^0}{\epsilon}$.
4. Continue with the remaining columns of $\mathbf{G}_{\mathrm{PNMPC}}$ using the same procedure as in the two previous steps. Notice that number of column of $\mathbf{G}_{\mathrm{PNMPC}}$ is determined by the control horizon N_u, so the last column is given by: $\mathbf{G}_{\mathrm{PNMPC}}(:,N_u)=\frac{\hat{\mathbf{Y}}^{N_u}-\hat{\mathbf{Y}}^0}{\epsilon}$.

[a]The algorithm has been described for the tank fast heating mode case, in which only one input is used. When two inputs are used, as in the normal operating mode case, this procedure must be repeated for each input, applying small increments at one of the input while the other one is kept constant, thus obtaining the formulation presented in Eq. 21-24.

5.2.1. Cost functions

In PNMPC controllers, the control signal is calculated by minimizing a cost function. In this case, three different cost functions have been formulated. It should be taken into account that the control architecture includes two control modes. Thus, the first cost function is the one used by the PNMPC strategy in the tank fast heating mode, whereas the other two are the ones proposed for the normal operating mode.

The tank fast heating mode cost function is aimed at finding out the actual and future control changes ($\mathbf{\Delta U}_{\mathrm{J1}} = \mathbf{TT2}_{\mathrm{SP}}$) maximizing **TT3** ($\hat{\mathbf{Y}}_{\mathrm{J1}}$):

$$\mathrm{J1} = -\sum_{j=1}^{N_1} \hat{Y}_{\mathrm{J1}}(k+j|k), \tag{25}$$

where N_1 is the prediction horizon and $\hat{Y}_{\mathrm{J1}}(k+j|k)$ is the prediction of TT3 at instant $k+j$, calculated with the information available at instant k.

The first cost function proposed for the normal operating mode tries to maximize **TT10** ($\hat{\mathbf{Y}}$) in order to increase the thermal efficiency and the distillate production, in accordance with the analysis presented in Section 4. This cost function also penalizes the future control changes $\mathbf{\Delta U}$ ($\mathbf{U_1}$=$\mathbf{TT2}_{\mathrm{SP}}$ and

$\mathbf{U_2}$=$\mathbf{FT2}_{\mathrm{SP}}$) by means of a weight factor λ_i:

$$\mathrm{J2} = -\sum_{j=1}^{N} \hat{Y}(k+j|k) + \sum_{i=1}^{2}\sum_{j=1}^{N_u} \lambda_i [\Delta U_i(k+j-1)]^2, \tag{26}$$

where N is the prediction horizon, N_u is the control horizon, $\hat{Y}(k+j|k)$ is the prediction of TT10 estimated at sample time $k+j$ with the information acquired up to discrete-time instant k, $\Delta U(k+j-1)$ is the future increment in the control variable i, where U_1 is $\mathrm{TT2_{SP}}$ and U_2 is $\mathrm{FT2_{SP}}$, and λ_1 and λ_2 are weigthing factors affecting $\mathbf{U_1}$ and $\mathbf{U_2}$ respectively.

The second cost function proposed for the normal operating mode provides the actual and future control changes $\mathbf{\Delta U}$ ($\mathbf{U_1}$=$\mathbf{TT2}_{\mathrm{SP}}$ and $\mathbf{U_2}$=$\mathbf{FT2}_{\mathrm{SP}}$) minimizing the relation between the distillate production ($\hat{D}$) [$\mathrm{m^3}$] and its associated electric costs ($\hat{E}_{Cost}$) [€]:

$$\mathrm{J3} = \sum_{j=1}^{N} \frac{\hat{E}_{Cost}(k+j|k)}{\hat{D}(k+j|k)}. \tag{27}$$

In this cost function, $\hat{D}_{Flux}(k+j|k)$ is estimated using the MD module model (Eq. 13), with the prediction of TT10 ($\hat{\mathbf{Y}}$) provided by the PNMPC strategy:

$$\begin{aligned}\hat{D}_{Flux}(k+j|k) = 24 \cdot (0.135 + 0.003 \cdot \hat{Y}(k+j|k) - 0.0204 \cdot \mathrm{TT11} - 0.001 \cdot \mathrm{FT4} \\ + 0.00004 \cdot \hat{Y}(k+j|k) \cdot \mathrm{FT4}),\end{aligned} \tag{28}$$

where TT11 and FT4 are constant at 20 ^{o}C and 600 L/h, respectively.

The electric costs associated to the operation can be divided in two parts, a fixed part that is not included in the cost function, produced by pumps which are operated with constant references (pump 3 and 4), and a variable part, included in the cost function, produced by pumps which are in charge of controlling TT2 and FT2 (pump 1 and 2). The electric power consumed by pumps is estimated with the characteristic pump curves provided by the manufacturer:

$$\mathrm{P_{Pump1}}(k+j|k)\ [\mathrm{kW}] = \frac{34.91 \cdot \mathrm{FT1}(k+j|k) \cdot 0.06 + 120}{1000}, \tag{29}$$

$$\mathrm{P_{Pump2}}(k+j|k)\ [\mathrm{kW}] = \frac{22.72 \cdot U_2(k+j|k) \cdot 0.06 + 39.54}{1000}. \tag{30}$$

Notice that the electric power consumption of pump 2 can be included directly in the optimization problem because it depends on one of the outputs ($\mathrm{FT2_{SP}}$). However, Eq. 29 depends on FT1 which is the control variable used to reach the other optimization output ($\mathrm{TT2_{SP}}$), so this equation must be rewritten in

terms of $TT2_{SP}$:

$$\begin{aligned} \mathrm{FT1}(k+j|k) = \Bigg[& \frac{\beta \cdot L_{eq}}{c_p \cdot (U_1(k+j|k) - \mathrm{TT1}(k+j|k))} \cdot \mathrm{I}(k+j|k) \\ & - \frac{H}{c_p} \cdot \frac{(\bar{T}(k+j|k) - \mathrm{T}_a(k+j|k))}{(U_1(k+j|k) - \mathrm{TT1}(k+j|k))} \Bigg] \cdot \frac{c_1}{\rho}, \end{aligned} \tag{31}$$

with

$$\bar{T}(k) = \frac{\mathrm{TT1}(k+j|k) + U_1(k+j|k)}{2}, \tag{32}$$

where TT1 and T_a are considered constants in the ahead instant times, whereas I is predicted with the method showed in Section 5.3. Finally, $\hat{E}_{Cost}$ is calculated as the product of the electric power consumed by pumps during N and the mean electricity price in Spain (0.14 €/kWh).

To solve the optimization problem, the *fmincon* solver of MATLAB has been chosen. This algorithm is based on the interior-point method, and it has been selected due to the problem being subjected to linear constraints (see next section) and it presents a smooth nonlinear behaviour.

5.2.2. Constraints

The cost functions presented in the previous section are subjected to three different kind of constraints. The first one, Eq. 33, limits the maximum and minimum changes allowed in the control signals (slew rate ones) at each sample time. These limits are imposed in order to obtain small setpoint movements trying to avoid security problems caused by transients. Thus, outlet solar field temperature steps are limited to 5 ^{o}C, whereas the steps in FT2 are limited to 1 L/min.

$$\begin{gathered} \mathbf{\Delta U}_{\min} \leq \mathbf{\Delta U}(\mathrm{k+j|k}) \leq \mathbf{\Delta U}_{\max} \\ j = 0, ..., N_u - 1. \end{gathered} \tag{33}$$

The second constraint, Eq. 36, defines the physical limits of the controlled variables. Pump 2 reachable ranges are 15-25 L/min. On the other hand, the maximun and minimun temperatures ($\mathrm{T}_{\max}$ and $\mathrm{T}_{\min}$) reachable by the solar field are not constants and vary in accordance with the operational conditions. To address this problem, these limits are calculated at each sample time, using a static version of the solar field model:

$$\mathrm{T}_{\min}(k) = \mathrm{TT1}(k) + \Big[\beta \cdot L_{eq} \cdot \mathrm{I}(k) - H \cdot (\bar{T}(k) - \mathrm{T}_a(k)) \Big] \cdot \frac{c_1}{\mathrm{FT1}_{\max} \cdot c_p \cdot \rho}, \tag{34}$$

$$\mathrm{T}_{\max}(k) = \mathrm{TT1}(k) + \Big[\beta \cdot L_{eq} \cdot \mathrm{I}(k) - H \cdot (\bar{T}(k) - \mathrm{T}_a(k)) \Big] \cdot \frac{c_1}{\mathrm{FT1}_{\min} \cdot c_p \cdot \rho}, \tag{35}$$

where $\mathrm{FT1_{min}}$ is 7.5 L/min and $\mathrm{FT1_{max}}$ is 16 L/min.

$$\begin{array}{rcl} \mathbf{U}_{\min} & \leq & \mathbf{U}(\mathrm{k+j|k}) \leq \mathbf{U}_{\max} \\ & j = 0, ..., N_u - 1. & \end{array} \tag{36}$$

Finally, the third constraint limits the output vector **TT10** to 80 ^{o}C that is the maximum temperature allowed by materials of the membranes. It should be taken into account that it is not necessary to limit **TT3** ($\hat{\mathbf{Y}}_{\mathrm{J1}}$) when the fast heating tank mode is used, since it is switched before reaching a high temperature (see Section 5.5).

$$\begin{array}{rcl} \mathrm{Y}_{\min} & \leq & \mathrm{Y}(\mathrm{k+j|k}) \leq \mathrm{Y}_{\max} \\ & j = 0, ..., N. & \end{array} \tag{37}$$

5.3. Irradiance estimation.

To complete the PNMPC strategy and to improve its performance, the irradiance behaviour is estimated by means of the DES technique (Pawlowski et al., 2011). Notice that ambient temperature could be also estimated with the same technique, however, it does not suffer significant changes along the sample time adopted. In this manner, the irradiance estimation is given by:

$$S_k = \alpha \cdot \mathrm{I}_k + (1 - \alpha) \cdot (S_{k-1} + b_{k-1}), \tag{38}$$

$$b_k = \theta \cdot (S_k - S_{k-1}) + (1 - \theta) \cdot b_{k-1}, \tag{39}$$

where S is the estimated series value, and b is the estimated trend, which are calculated using actual and past series values. The constants α and $\theta \in$ (0,1) have been characterized by means of optimization techniques using experimental irradiance values. Thus, the estimation of m periods is given by:

$$\hat{\mathrm{I}}_{k+m} = S_k + m \cdot b_k. \tag{40}$$

Several methods can be employed to set the initial values for S and b according to NIST (2006). In this case:

$$S_o = \mathrm{I}_k, \tag{41}$$

$$b_o = \frac{1}{3} \sum_{j=0}^{2} \mathrm{I}_{k-j} - \mathrm{I}_{k-j-1} \tag{42}$$

It should be considered that this forecasting irradiance method calculates N future values according to the prediction horizon of the PNMPC controller. Hence, to reconstruct the signal according to the sample time of the lower layer, the Lagrange interpolation method has been employed, in consonance with the ideas presented in (Pawłowski et al., 2014). Thus, supposing that the discrete

data set is composed by N samples, such as $\{(t_0, \mathrm{I}_0), ...(t_N, \mathrm{I}_N)\}$, the Lagrange polynomial applied to this problem is given by:

$$L(t) = \sum_{j=0}^{k} \mathrm{I}_j \cdot l_j, \tag{43}$$

where

$$l_j(t) = \prod_{i=0, i\neq j}^{k} \frac{t - t_i}{t_j - t_i} = \frac{t - t_0}{t_j - t_0} ... \frac{t - t_{j-1}}{t_j - t_{j-1}} \frac{t - t_{j+1}}{t_j - t_{j+1}} ... \frac{t - t_k}{t_j - t_k}. \tag{44}$$

5.4. Start-stop procedure

Based on the facility configuration and in the MD module operating limits (see Section 2.3), a start-stop procedure has been developed for the solar field and the MD module.

Due to irradiance conditions, TT2 can be lower than the tank temperature, causing the tank to cool down. To avoid this situation, the static model of the solar field is used to estimate the global irradiance value which ensures that TT2 is going to be higher that the tank temperature:

$$\mathrm{I}(k) = \left[\frac{\mathrm{FT1}(k) \cdot \rho}{c_1} + \frac{H}{c_p} \cdot \frac{\bar{T}(k) - \mathrm{T}_a(k)}{\mathrm{TT2}(k) - \mathrm{TT1}(k)} \right] \cdot \frac{c_p \cdot (\mathrm{TT2}(k) - \mathrm{TT1}(k))}{\beta \cdot L_{eq}}, \tag{45}$$

where TT2 is fixed at the same value as the top tank temperature and TT1 at the same value as the bottom tank temperature. Therefore, pump 1 is tuned on or off if the real irradiance value is higher or lower than the calculated one. This condition is evaluated each 5 min, in accordance with the sample time of the PNMPC strategy (see Section 6). Furthermore, to avoid chattering problems, a mean irradiance value of the last 10 min sampled each second is used.

In the same way, as it has been previously commented, it does not makes sense to operate the MD module with temperatures lower than 60 ^{o}C. To tackle this problem, the heat exchanger model has been used to calculate if the tank temperature allows to operate the MD module over 60 ^{o}C:

$$\mathrm{TT6_m}(k) = \mathrm{TT5}(k) - \eta_{he,1} \cdot (\mathrm{TT5}(k) - \mathrm{TT9}(k)), \tag{46}$$

$$\mathrm{TT5_m}(k) = \frac{\mathrm{TT10_{min}}(k) - \mathrm{TT9}(k) + \eta_{he,2} \cdot \mathrm{TT6_m}(k)}{\eta_{he,2}}. \tag{47}$$

where it is assumed that TT5 has the same value as the top tank temperature and $\mathrm{TT10_{min}}$ is equal to 60 ^{o}C. TT9 is calculated with ΔT model (Eq. 14). Hence, pump 2, 3 and 4 are turned on or off whether $\mathrm{TT5_m}$ is respectively higher or lower than the tank temperature. This condition is also executed with a sample time of 5 min.

5.5. Decision maker

The aim of this block (see Fig. 6) is to switch between the two proposed control modes. Thus, this block selects the fast heating tank mode or the normal operating mode according to the following situations:

1. The tank temperature does not allow to operate the MD module over 60 ^{o}C. Thus, the start-stop procedure is in charge of turning on pump 1 according to the irradiance level, and this block selects the fast heating tank mode, which activates the optimization problem related to J1 (see Eq. 25).
2. The global irradiance level permits to obtain an outlet solar field temperature higher than the tank temperature, and the tank temperature allows to operate the MD module over 60 ^{o}C. In this situation, the start-stop procedure turns on pumps 1, 2, 3 and 4 and the decision maker selects the normal operating mode, cost functions J2 or J3 (see Eq. 26, 27).
3. The solar field cannot be operated with a temperature higher than the tank temperature, but the tank temperature allows to operate the MD module over 60 ^{o}C. Consequently, the start-stop procedure only turns on pump 2, 3 and 4, and the decision maker selects the normal operating mode. It should be stressed that, in this situation, the PNMPC strategy only provides setpoint for FT2, maintaining $TT2_{SP}$ equal to 0.

6. Simulation results

This section presents the simulation results obtained with the proposed control system, during a week with variable weather profiles. Fig. 9 shows the meteorological data from PSA used in the tests, corresponding to the days of March 6 to 12, 2017. Firstly, the control system performance is analyzed, making a comparison between the performance of the two control objective functions formulated for the normal operating mode. Secondly, the results obtained with the proposed control architecture are compared with a case in which only the direct control layer is employed with constant references. In addition, two potential industrial applications are suggested in order to evidence the benefits achieved with the proposed hierarchical control system in terms of thermal efficiency and cost savings.

The tests have been carried out with a sample time of 5 min in the upper layer and 5 s in the lower one. The control and prediction horizon in both modes, the fast heating tank mode and the normal operating mode, were 2. These values have been selected taking into account the closed-loop characteristic time constant of the solar field controller, the characteristic time constant of the intermediate buffer (tank) and the heat exchanger, and chattering problems observed in pump 1 when small values of the sample time are used and the start-stop procedure is evaluated. On the other hand, the use of a larger prediction horizon implies higher errors in the irradiance prediction, leading to inaccurate control actions. Besides, lower sample times have been tested without improving the results obtained with a sample time of 5 min. The weighting

factor values adopted in J2 were λ_1=0.1 and λ_2 = 1.1, decided after simulating different combinations, while the DES technique parameters were α=0.1 and θ=0.9. Besides, FT4 has been fixed at 600 L/h, according to the study presented in Section 4, and FT3 is operated at the same value in order to achieve a maximun heat transfer in the heat exchanger.

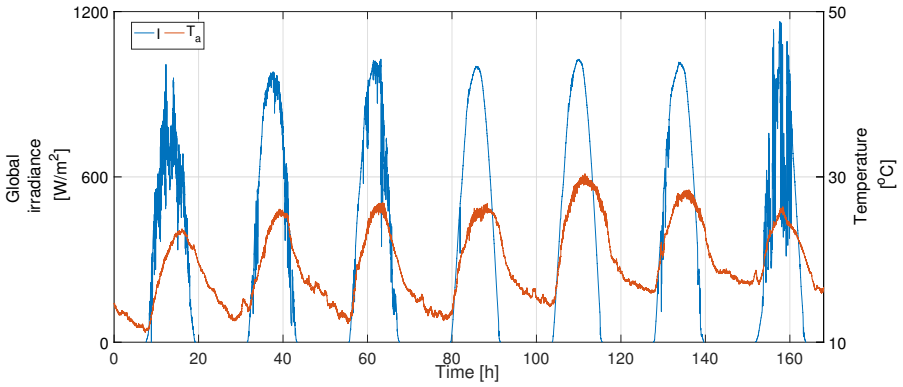

Figure 9: Meteorological data from PSA.

6.1. Control system performance

In order to compare the performance of the hierarchical control system with the two objective functions proposed for the normal operating mode, the last simulation day is shown in Fig. 10 and 11 for J2 and J3 respectively.

The start-stop procedure enables that, at the beginning of the operation, the initial tank temperature is similar all the days, since the start and stop conditions are the same, as it has been previously mentioned in Section 5.4. Thus, the operation in both cases starts at instant time 153.9 h. As the tank temperature is not high enough to operate the MD module, the decision maker selects the fast heating tank mode. Initially, this mode provides $TT2_{SP}$ close to the lower optimization temperature limit (normal behaviour in clear sky days), when FT1 is close to the maximum, to increase the water flow rate and increase the thermal power delivered to the tank. However, this operation is subjected to strong irradiance disturbances, so that, $TT2_{SP}$ and therefore FT1 vary according to disturbances. At instant 154.4 h, the start-stop procedure turns off pump 1 because the irradiance level is too low. After 12 min, pump 1 is turned on and the control system uses the fast heating tank mode to continue augmenting the tank temperature. It must be kept in mind that, in this kind of days, if the condition to turn on and off pump 1 was checked with instant irradiance values rather than mean ones, chattering problems might occur. In this way, even though the outlet solar field temperature is lower than the top tank temperature (TT3) in short time periods, the operation is more efficient and continuous.

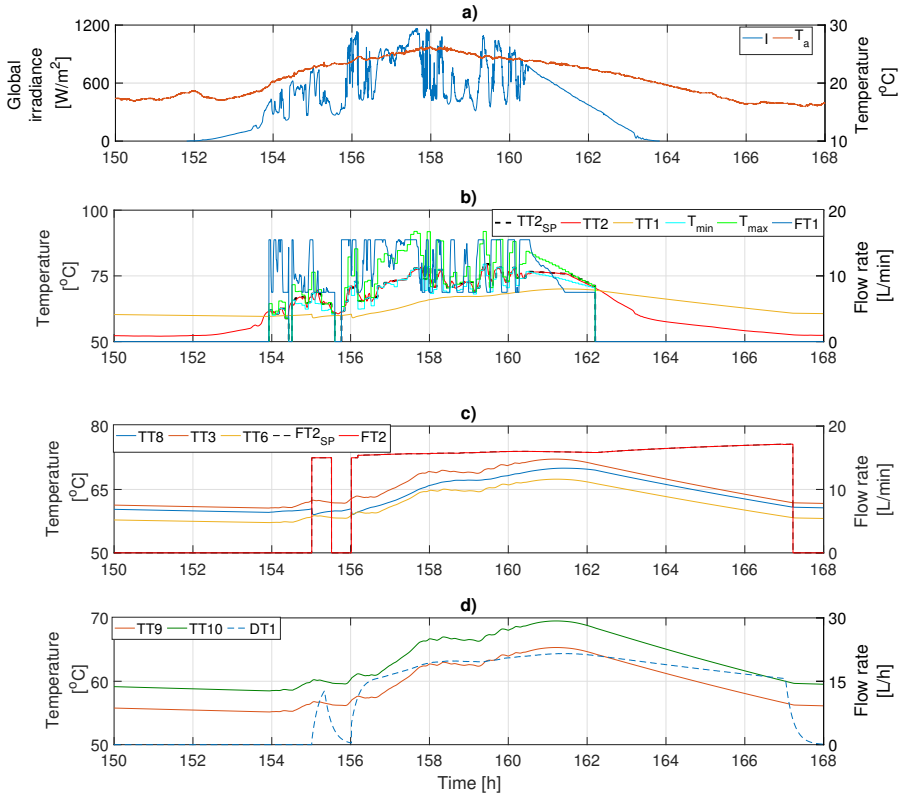

Figure 10: Control system performance with J2. a) meteorological conditions, b) solar field variables, c) tank and distribution system variables and d) MD module variables.

At instant 155 h, the tank temperature reaches 62.4 ^{o}C which is high enough to operate the MD module over 60 ^{o}C. From this moment the operation is different in both cases, due to the fact that decision maker selects the normal operating mode. Notice that in a clear sky day, when using J2, $TT2_{SP}$ is operated as in the fast heating mode (close to the T_{min} curve) whereas $FT2_{SP}$ is almost constant at the minimum when the solar field is used, and it is smoothly increased when the solar field is turned off. This increase is justified because, when the solar field is turned off and the tank temperature is high, the control system tries to keep the thermal energy stored in the tank, by maintaining as much as possible the temperature of the mixture produced in the distribution system (TT7). This procedure is displayed in Fig. 10 and 11.

On the other hand, when using J3, $TT2_{SP}$ is operated close to the upper limit (which causes FT1 to be close the minimum). Thus, the electric energy consumption of pump 1 is lower. Conversely, $FT2_{SP}$ is not operated at the minimum when the solar field is operating, as happens when using J2, since

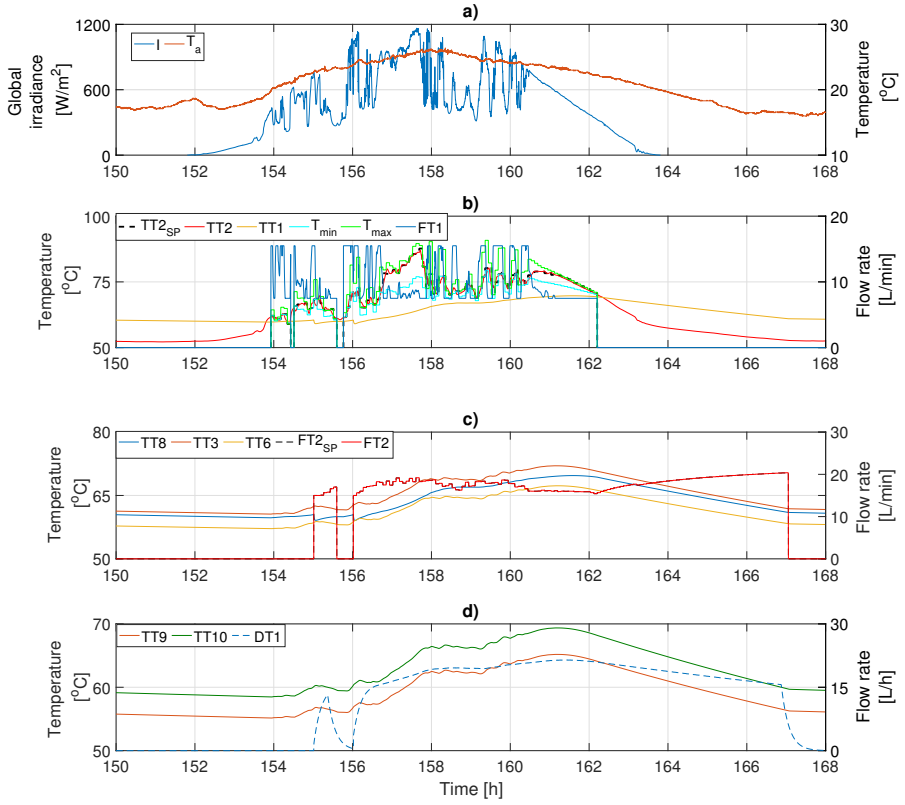

Figure 11: Control system performance with J3. a) meteorological conditions, b) solar field variables, c) tank and distribution system variables and d) MD module variables.

it varies in accordance with the operational conditions trying to increase the thermal energy stored in the tank. It should be taken into account that the electric consumption of pump 1 is higher than that of pump 2 (see Eq. 29 and 30), in this way, the control system mainly acts over $FT2_{SP}$ to increase the distillate production. Then, when the solar field is not operated, $FT2_{SP}$ is smoothly increased again, as when J2 is used.

The operational procedure described previously can be observed in Fig. 10 and 11, but in this occasion the references experiment more changes due to irradiance variation. At instant 155.56 h and 155.55 h in Fig. 10 and 11 respectively, the solar field and the MD module are turned off because of strong disturbances. After 16 min, the operation is reestablished carrying on with the normal control operating procedure.

6.2. Comparison of results and discussion

Tab. 4 shows the comparison between the results obtained with the hierarchical control architecture, adopting different prediction horizons in the normal operating mode, and the ones obtained using only the direct control layer with $TT2_{SP}$ equal to 85 ^{o}C and $FT2_{SP}$ equal to 25 L/min. The stored distillate production during the seven days, supposing that it is not removed at the end of the operation, the mean STEC and the mean electric costs per volume unit of distillate in the seven days have been employed as performance indexes. Besides, the MD module operating hours (MD-OH) are also reported.

As can be observed in Tab. 4, all the performance parameters are improved by using the proposed hierarchical control system. One of the main advantages is that the PNMPC strategy permits to operate the MD module for longer time, between 30-40 min each day, depending on the objective function used in the normal operating mode. This fact, together with the increase of the evaporator inlet temperature, causes the distillate production to augment between 14-20 L each day. Notice that, in terms of distillate production, the results obtained with J2 are the best, as was expected.

PNMPC	N	MD-OH[h]	Distillate [L]	STEC [kWh/m^3]	Costs [€/m^3]
No	-	97.49	1945	140.17	1.48
J2	2	102.50	2082	138.96	1.36
	3	102.47	2073	139.01	1.37
	4	102.42	2074	138.99	1.35
J3	2	100.50	2043	139.31	1.34
	3	100.83	2021	139.52	1.35
	4	101.33	2018	139.76	1.35

Table 4: Comparison of simulation results

Moreover, the mean STEC is also diminished in all the cases. It should be considered that STEC is an index that varies in accordance with the temperature. In this manner, although the optimum operation point is achieved working at the maximum temperature, when operating only with solar energy, the STEC tendency varies according to the irradiance behaviour. Thus, at the beginning of the operation the STEC value is high, around the solar midday when the thermal energy of the tank is maximum, STEC reaches its minimum value, and at the end of the operation when the thermal energy of the tank drops, STEC increases. It should be also taken into account that, as the PNMPC strategy makes the operation longer, working at low temperature during more time, the mean STEC value is penalized. Nevertheless, the STEC value is clearly improved, obtaining the best result by using J2 with N=2 as expected, that provides a mean value of 1.21 kWh/m^3 less than the case without the PNMPC strategy, which means that the proposed technique requires 1.21 kWh of thermal energy less to produce a volume unit of distillate.

In order to highlight STEC improvements and to compare in the same conditions both cases, a simulation has been carried out using the second day of

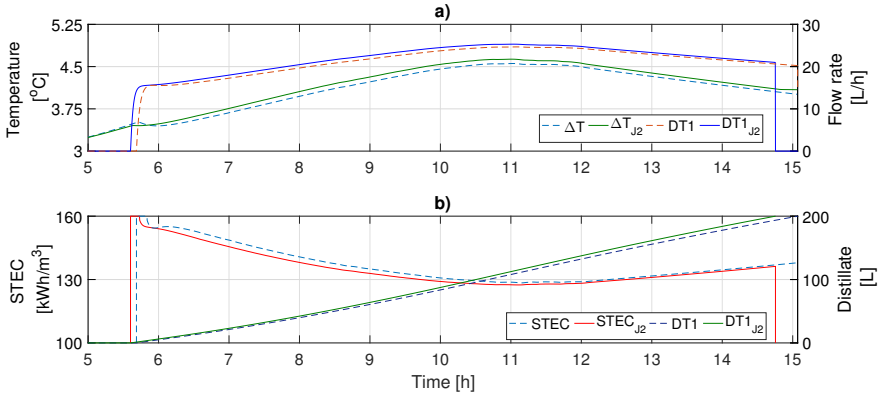

Figure 12: STEC calculation. a) variables affecting STEC, and b) STEC and accumulative distillate production.

meteorological data (see Fig. 9), establishing as stopping condition a distillate production of 200 L. Fig. 12 shows the variables affecting STEC for the case with PNMPC strategy (the ones with the subscript J2) using J2 with N=2, and for the case without PNMPC strategy. As it has been discussed in Section 4, an increase in the evaporator inlet temperature (TT10) causes an augment in ΔT and the distillate production. According to Eq. 15, the increase of ΔT produces higher values of STEC, however, this increase is almost insignificant in comparison with the one achieved in the distillate production, thus minimizing STEC as can be observed in Fig. 12. Therefore, the use of the PNMPC strategy enables the STEC to be almost 3 kWh/m^3 lower than the case without PNMPC while the solar field is used, and around 0.8 kWh/m^3 when the solar field is not operative. This fact evidences that the PNMPC strategy manages properly the solar energy, obtaining the maximum temperature reachable at each moment, and enabling the MD module to operate with a high thermal efficiency.

In addition, Fig. 12 highlights how the PNMPC strategy allows starting operation before, thanks to the fast heating tank mode, and reaches the desired distillate production before, thanks to the solar energy management produced by normal operating mode.

From an economic point of view, the results obtained are quite significant. Notice that to calculate the cost index, the fixed costs associated to the operation of pump 3 and 4 have not been taken into account. In the same way, it should be pointed out that, in the pilot facility pumps are oversized, so the absolute value of the electric costs presented in Tab. 4 are high, however the relative ones are valid. Thus, when J3 is used with N=2 in the normal operating mode, 0.14 € per m^3 of distillate produced can be saved.

At this point, it is important to mention that the SMD facility is a small-scale pilot plant one. In potential industrial cases the improvements in terms of thermal efficiency and economic costs can be very relevant. Consider the

following two potential applications of MD technology:

1. Offgrid areas water supply. One of the main future application of SMD processes is the fresh water supply in offgrid areas with sea or brackish water access. In Spain, an inhabitant has an average water consumption of 142 L/day (Instituto nacional de estadística, 2013). In this way, in a small area of 3654 inhabitants, population of Tabernas (Almería) where the pilot facility is located, the use of the proposed control system, with J3 and N=2, can save around 26514.15 € each year in comparison with an operation without PNMPC. In addition, the plant would require around 627.83 kWh less thermal energy each day, by using J2 with N=2.
2. Crops water supply. An other potential application is to use MD technology to fulfil the irrigation water demand of cultivation areas close to the coast. According to the studio presented in Becerra & Bravo (2010), tomato crop growth, one of the most extended in the south of Spain, has a water demand of 4.11 m^3/ha. Assuming a cultivation area of 20 ha (typical of small-medium size farmers in Almería, south of Spain), the use of the proposed control architecture, with J3 and N=2, can save around 4200.42 € each year, requiring around 99.46 kWh less thermal energy each day if J2 with N=2 is employed.

7. Experimental results

An experimental campaign has been carried out to evaluate the performance of the hierarchical control system in the SMD plant at PSA during March 2017. Figures 13, 14 and 15 show the most representative results. The control system configuration employed in these tests is the same that the one used in the simulation tests (Section 6.1).

Firstly, Fig. 13 presents a test using J2 in a clear sky day. The operation starts at 10.85 h, using the normal operating mode since the tank temperature and irradiance level permit to operate the MD module and the solar field. As happened in simulation when using J2, $TT2_{SP}$ is close to the lower limit, thus maintaining FT1 at maximum and augmenting the thermal power delivered from the solar field to the tank (see Fig. 13b and c). On the other hand, $FT2_{SP}$ is kept close to the minimum. As there are not disturbances in the global irradiance, the operating evaporator temperature inside the module (TT10) increases over the course of the operation. At instant 14.8 h, TT10 reaches 79 ^{o}C, as can be observed in Fig. 13d, close to the temperature limit (80 ^{o}C) which can cause damage in the module membrane. Due to the fact that this limit is included in the optimization problem constraints, the algorithm increases $TT2_{SP}$, so that, FT1 decreases and the tank temperature is almost constant around 15.5 h. This action helps controlling the evaporator inlet temperature TT10, thus preventing it to reach 80 ^{o}C, as can be seen in Fig. 13d. Notice that in this test, the maximum distillate production (see Fig. 13d) reached is 30 L/h.

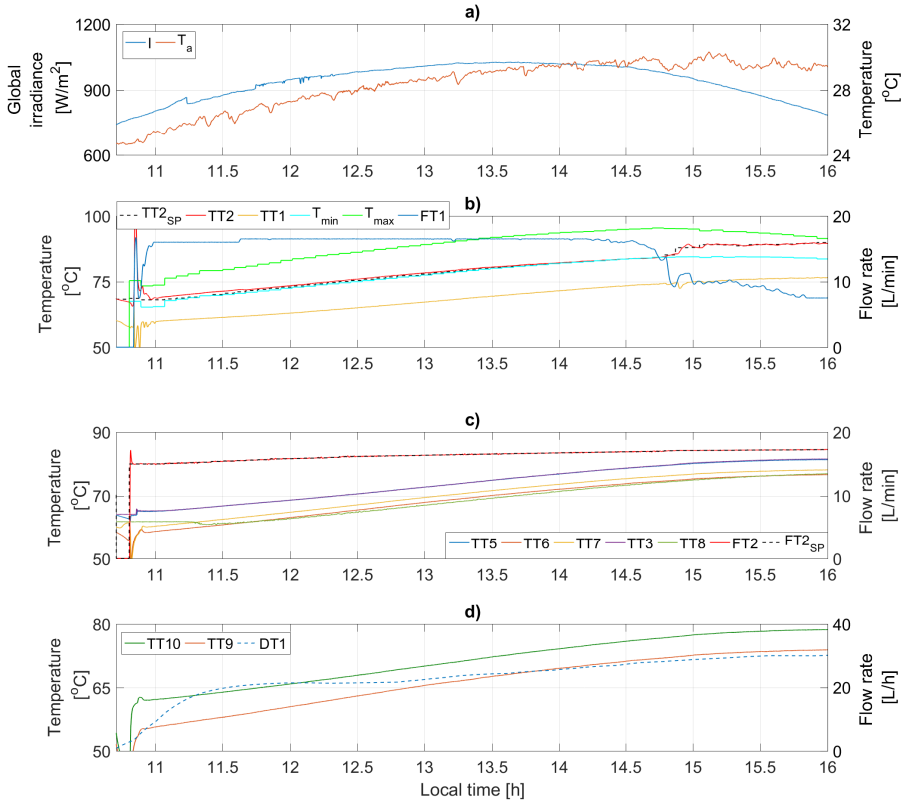

Figure 13: Experimental results with J2 in a clear sky day. a) meteorological conditions, b) solar field variables, c) tank and distribution system variables and d) MD module variables.

Secondly, Fig. 14 shows another test using J2 in the normal operating mode, but in this occasion there are irradiance disturbances caused by passing clouds. The operation starts at 9.85 h, using the fast heating tank mode because the tank temperature is not high enough to operate the MD module over 60 ^{o}C. As the tank temperature at the beginning is too low, the algorithm generates references close to T_{min}, thus maximizing the tank temperature working with FT1 close to the maximum. At instant 10.5 h, $TT2_{SP}$ begins to approach the lower limit, thus augmenting FT1, however, at 10.7 h irradiance disturbances cause the control algorithm to increase $TT2_{SP}$ again (see Fig. 14b).

At 11.26 h, the tank temperature reaches 63 ^{o}C and the MD module is turned on. In this moment, the inlet solar field temperature decreases due to cold re-circulating fluid being introduced in the lower part of the tank, so that, FT1 decreases to maintain the desired reference $TT2_{SP}$. Then, from 11.4 to 12 h, $TT2_{SP}$ and FT1 vary according to irradiance disturbances (see Fig. 14b). In the same way, during this time period, $TT2_{SP}$ approaches the lower limit, thus

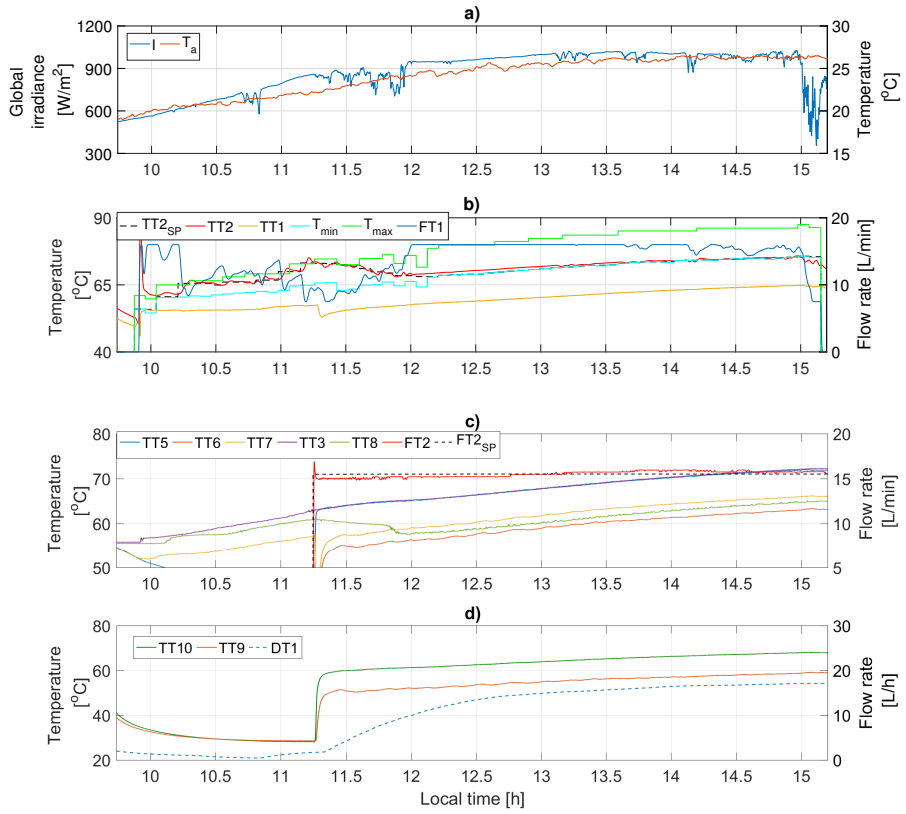

Figure 14: Experimental results with J2 in a cloudy day. a) meteorological conditions, b) solar field variables, c) tank and distribution system variables and d) MD module variables.

increasing FT1, as expected in a normal operation (clear sky conditions). Until 15 h, the operation continues with this procedure, nevertheless, it should be remarked that FT1 experiments variations because of irradiance disturbances. Finally, at 15 h the irradiance level varies strongly, therefore FT1 decreases until saturating. As the strong irradiance disturbances lasts more than 10 min (see Fig. 14b), the mean irradiance value during this period abruptly decreases, thereby, the start-stop procedure turns off the solar field. Notice that, although the solar field is turned off, the MD module is kept operating (see Fig. 14c and d) since the tank temperature enables the module to operate over 60 ^{o}C.

Thirdly, Fig. 15 shows a test using J3 in the normal operating mode. As in the previous case, at the beginning of the operation the tank temperature is low, so the decision maker selects the fast heating tank mode. In this way, as there are not irradiance disturbances and the tank temperature is not as low as in the previous case, the algorithm keeps $TT2_{SP}$ close to the lower limit

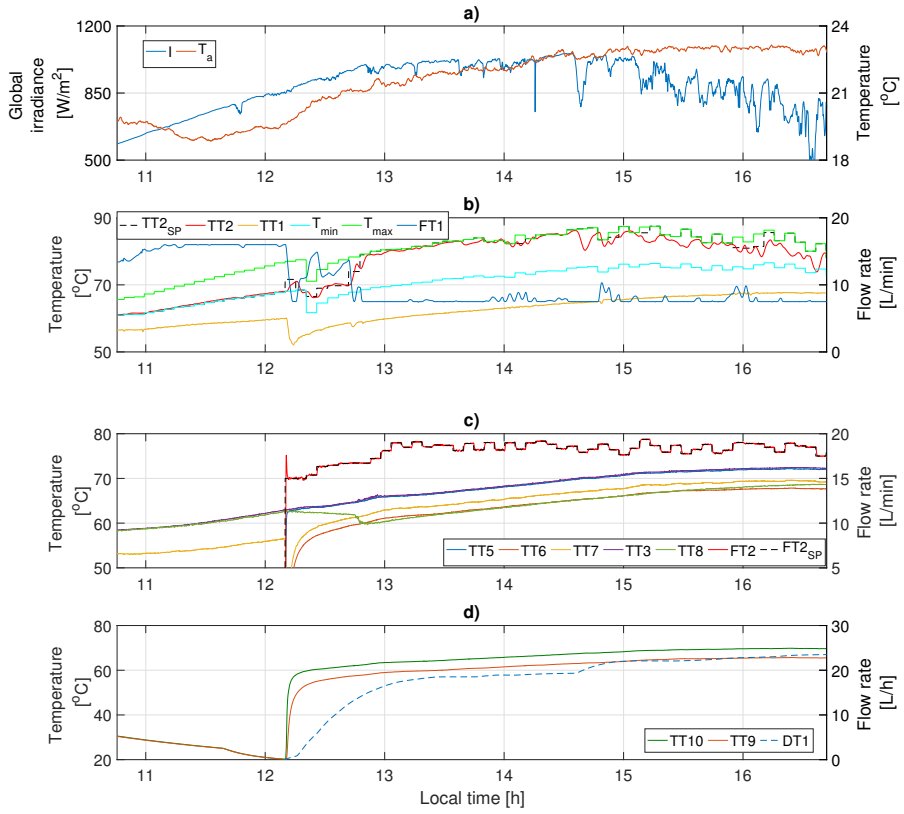

Figure 15: Experimental results with J3 in a cloudy day. a) meteorological conditions, b) solar field variables, c) tank and distribution system variables and d) MD module variables.

as expected in a clear sky operation day. Then, at 12.4 h, the decision maker changes to the normal operating mode, at this point, the inlet solar field temperature strongly decreases, due to the fact that cold fluid coming from the distribution system is introduced in the lower part of the tank. In this way, according to Eq. 35 and **??** the optimization temperature limits, and therefore $TT2_{SP}$, decrease (see Fig. 15b). Then, according to the simulation tests with J3, the control algorithm varies $FT2_{SP}$ in accordance with disturbances and $TT2_{SP}$, trying to maximize the thermal energy stored in the tank, as it can be observed in Fig. 15c. It should be mentioned that, in this kind of days with large irradiance variations, there are some periods in which the references calculated by the upper layer cannot be reached by the lower one, as can be observed in Fig. 15 from 14.5 h. Although the method presented in Section 5.2.2 to calculate the maximum and minimum temperatures reachable by the solar field provides reliable results, it is based on a static model and some errors are obtained when sudden disturbances occur such as in the case of irradiance in cloudy days. This

fact is specially remarkable when using J3, since this objective function tries to maintain FT1 close to the lower limit to minimize the costs, and the solar field controller is saturated or close to saturation, so it is not able to reach or regulate around the setpoint.

8. Conclusions

This work focuses on optimizing the solar-powered operation of a MD facility in terms of distillate production, thermal energy and economic costs, taking into account the intermittent availability of energy caused by the use of solar energy as source. To deal with this problem, a hierarchical control system composed by two layers is proposed. The upper layer is based on a PNMPC controller that includes an optimization problem, whereas the inner one consists on a direct control system formed by PI plus feedforward controllers. In addition, two control modes and a start-stop procedure have been developed to complete the hierarchical control system.

The proposed control system has been tested in simulation, in the nonlinear test-bed model, and experimentally, in the solar-MD pilot plant at PSA. The results obtained in the pilot plant, show that the proposed control system is able to improve the daily distillate production in 14-20 L, reduce the thermal energy demand in 0.41-1.21 kWh/m^3 and diminish the costs in 0.11-0.14 €/m^3, depending on the objective function adopted in the PNMPC strategy. These results have been extrapolated to two real potential applications of MD technology, evidencing that the control system can save around 26514 €/year and 627.83 kWh/m^3 in the supply of a small representative area of 3654 inhabitants, and 4200.42 €/year and 99.46 kWh/m^3 in the supply of a greenhouse tomato growth area of 20 ha.

In future works, the proposed control architecture will be extended to the non renewable resources, in order to undertake the night operation of the facility. Then, the full control strategy will be integrated in an optimization problem that allows to obtain an optimal design of a SMD facility, according to the water demand of the application scenario.

Acknowledgments

This work has been funded by the National R+D+i Plan Project DPI2014-56364-C2-1/2-R of the Spanish Ministry of Economy, Industry and Competitiveness and ERDF funds.

References

Alkhudhiri, A., Darwish, N., & Hilal, N. (2012). Membrane distillation: a comprehensive review. *Desalination*, *287*, 2–18.

Álvarez, J., Redondo, J., Camponogara, E., Normey-Rico, J., Berenguel, M., & Ortigosa, P. (2013). Optimizing building comfort temperature regulation via model predictive control. *Energy and Buildings*, *57*, 361–372.

Andrade, G., Pagano, D., Álvarez, J., & Berenguel, M. (2013). A practical nmpc with robustness of stability applied to distributed solar power plants. *Solar Energy*, *92*, 106–122.

Becerra, A. T., & Bravo, X. L. (2010). La agricultura intensiva del poniente almeriense. diagnóstico e instrumentos de gestión ambiental. *M+ A. Revista Electrónica de Medioambiente*, (pp. 18–40).

de la Calle, A., Roca, L., Bonilla, J., & Palenzuela, P. (2016). Dynamic modeling and simulation of a double-effect absorption heat pump. *International Journal of Refrigeration*, *72*, 171–191.

Castilla, M., Álvarez, J., Normey-Rico, J., & Rodríguez, F. (2014). Thermal comfort control using a non-linear mpc strategy: A real case of study in a bioclimatic building. *Journal of Process Control*, *24*, 703–713.

Chang, H., Lyu, S.-G., Tsai, C.-M., Chen, Y.-H., Cheng, T.-W., & Chou, Y.-H. (2012). Experimental and simulation study of a solar thermal driven membrane distillation desalination process. *Desalination*, *286*, 400–411.

Chang, H., Wang, G.-B., Chen, Y.-H., Li, C.-C., & Chang, C.-L. (2010). Modeling and optimization of a solar driven membrane distillation desalination system. *Renewable Energy*, *35*, 2714–2722.

Cipollina, A., Di Sparti, M., Tamburini, A., & Micale, G. (2012). Development of a membrane distillation module for solar energy seawater desalination. *Chemical Engineering Research and Design*, *90*, 2101–2121.

Duffie, J. A., & Beckman, W. A. (1980). *Solar engineering of thermal processes*. John Wiley and Sons, New York, NY.

Duong, H. C., Cooper, P., Nelemans, B., Cath, T. Y., & Nghiem, L. D. (2016). Evaluating energy consumption of air gap membrane distillation for seawater desalination at pilot scale level. *Separation and Purification Technology*, *166*, 55–62.

Gil, J. D., Ruiz-Aguirre, A., Roca, L., Zaragoza, G., & Berenguel, M. (2015a). Solar membrane distillation: A control perspective. In *23th Mediterranean Conference on Control and Automation (MED 2015)* (pp. 796–802). Torremolinos, Málaga, Spain.

Gil, J. D., Ruiz-Aguirre, A., Roca, L., Zaragoza, G., Berenguel, M., & Guzmán, J. L. (2015b). Control de plantas de destilación por membranas con apoyo de energía solar–parte 1: Esquemas (Control of membrane distillation plants with solar energy support - part 1: Schema). In *XXXVI Jornadas Automática, Bilbao, España*.

Gil, J. D., Ruiz-Aguirre, A., Roca, L., Zaragoza, G., Berenguel, M., & Guzmán, J. L. (2015c). Control de plantas de destilación por membranas con apoyo de energía solar–parte 2: Resultados (Control of membrane distillation plants with solar energy support - part 2: Results). In *XXXVI Jornadas Automática, Bilbao, España*.

Guillén-Burrieza, E., Zaragoza, G., Miralles-Cuevas, S., & Blanco, J. (2012). Experimental evaluation of two pilot-scale membrane distillation modules used for solar desalination. *Journal of Membrane Science*, *409*, 264–275.

He, Q., Li, P., Geng, H., Zhang, C., Wang, J., & Chang, H. (2014). Modeling and optimization of air gap membrane distillation system for desalination. *Desalination*, *354*, 68–75.

Instituto nacional de estadística (2013). `http://www.ine.es/prensa/np807.pdf`.

Karam, A. M., & Laleg-Kirati, T. M. (2015). Real time optimization of solar powered direct contact membrane distillation based on multivariable extremum seeking. In *Control Applications (CCA), 2015 IEEE Conference on* (pp. 1618–1623). IEEE.

Khayet, M., & Cojocaru, C. (2012). Air gap membrane distillation: Desalination, modeling and optimization. *Desalination*, *287*, 138–145.

NIST (2006). Engineering statistics handbook. URL `http://www.itl.nist.gov/div898/handbook/`.

Pawłowski, A., Guzmán, J. L., Berenguel, M., & Dormido, S. (2014). Lagrange interpolation for signal reconstruction in event-based GPC. In *Emerging Technology and Factory Automation (ETFA), 2014 IEEE* (pp. 1–7). IEEE.

Pawlowski, A., Guzmán, J. L., Rodríguez, F., Berenguel, M., & Normey-Rico, J. E. (2011). Predictive control with disturbance forecasting for greenhouse diurnal temperature control. *IFAC Proceedings Volumes*, *44*, 1779–1784.

Plucenio, A., Pagano, D., Bruciapaglia, A., & Normey-Rico, J. (2007). A practical approach to predictive control for nonlinear processes. *IFAC Proceedings Volumes*, *40*, 210–215.

Porrazzo, R., Cipollina, A., Galluzzo, M., & Micale, G. (2013). A neural network-based optimizing control system for a seawater-desalination solar-powered membrane distillation unit. *Computers & Chemical Engineering*, *54*, 79–96.

Roca, L., Guzman, J. L., Normey-Rico, J. E., Berenguel, M., & Yebra, L. J. (2009). Robust constrained predictive feedback linearization controller in a solar desalination plant collector field. *Control Engineering Practice*, *17*, 1076–1088.

Ruiz-Aguirre, A., Alarcón-Padilla, D. C., & Zaragoza, G. (2015). Productivity analysis of two spiral-wound membrane distillation prototypes coupled with solar energy. *Desalination and Water Treatment*, *55*, 2777–2785.

Ruiz-Aguirre, A., Andrés-Mañas, J., Fernández-Sevilla, J., & Zaragoza, G. (2017a). Comparative characterization of three commercial spiral-wound membrane distillation modules. *Desalination and Water Treatment*, *61*, 152–159.

Ruiz-Aguirre, A., Andrés-Mañas, J., Fernández-Sevilla, J., & Zaragoza, G. (2017b). Modeling and optimization of a commercial permeate gap spiral wound membrane distillation module for seawater desalination. *Desalination*, *419*, 160–168.

Zaragoza, G., Ruiz-Aguirre, A., & Guillén-Burrieza, E. (2014). Efficiency in the use of solar thermal energy of small membrane desalination systems for decentralized water production. *Applied Energy*, *130*, 491–499.